

# Insights on the fundamental lithium storage behavior of all-solid-state lithium batteries containing the $\text{LiNi}_{0.8}\text{Co}_{0.15}\text{Al}_{0.05}\text{O}_2$ cathode and sulfide electrolyte

Gang Peng<sup>a, b</sup>, Xiayin Yao<sup>a, \*\*</sup>, Hongli Wan<sup>a</sup>, Bingxin Huang<sup>a</sup>, Jingyun Yin<sup>a</sup>, Fei Ding<sup>b</sup>, Xiaoxiong Xu<sup>a, \*</sup>

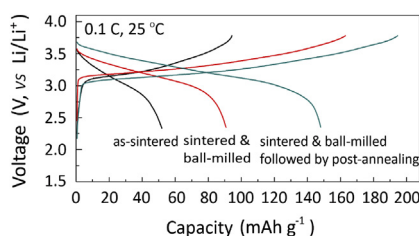
<sup>a</sup> Ningbo Institute of Materials Technology and Engineering, Chinese Academy of Sciences, 315201, Ningbo, PR China

<sup>b</sup> National Key Laboratory of Power Sources, Tianjin Institute of Power Sources, 300381, Tianjin, PR China

## HIGHLIGHTS

- Fundamental lithium storage behavior of solid-state battery with NCA is investigated.
- The relationship between electrochemical performances and structure is revealed.
- Particle size, surface impurities and defects affect the interfacial resistance.
- A ball-milling followed by post-annealing is demonstrated to improve performances.
- The NCA in  $\text{NCA}/\text{Li}_{10}\text{GeP}_2\text{S}_{12}/\text{Li-In}$  cell exhibits a discharge capacity of  $146 \text{ mAh g}^{-1}$ .

## GRAPHICAL ABSTRACT



## ABSTRACT

An insightful study on the fundamental lithium storage behavior of all-solid-state lithium battery with a structure of  $\text{LiNi}_{0.8}\text{Co}_{0.15}\text{Al}_{0.05}\text{O}_2$  (NCA)/ $\text{Li}_{10}\text{GeP}_2\text{S}_{12}$ /Li-In is carried out in this work. The relationship between electrochemical performances and particle size, surface impurities and defects of the NCA positive material is systematically investigated. It is found that a ball-milling technique can decrease the particle size and remove surface impurities of the NCA cathode while also give rise to surface defects which could be recovered by a post-annealing process. The results indicate that the interfacial resistance between the NCA and  $\text{Li}_{10}\text{GeP}_2\text{S}_{12}$  is obviously decreased during the ball-milling followed by a post-annealing. Consequently, the discharge capacity of NCA in the  $\text{NCA}/\text{Li}_{10}\text{GeP}_2\text{S}_{12}/\text{Li-In}$  solid-state battery is significantly enhanced, which exhibits a discharge capacity of  $146 \text{ mAh g}^{-1}$  at  $25^\circ\text{C}$ .

## Article history:

Received 28 August 2015

Received in revised form

25 December 2015

Accepted 11 January 2016

Available online 1 February 2016

## Keywords:

$\text{LiNi}_{0.8}\text{Co}_{0.15}\text{Al}_{0.05}\text{O}_2$  cathode

Post-annealing

Surface defects

$\text{Li}_{10}\text{GeP}_2\text{S}_{12}$  solid electrolyte

All-solid-state lithium batteries

## 1. Introduction

Lithium ion batteries have been widely used in portable electronic devices, such as laptops and cell phones [1]. The developing electric vehicles and energy storage devices for power stations have

\* Corresponding author.

\*\* Corresponding author.

E-mail addresses: [yaaxy@nimte.ac.cn](mailto:yaaxy@nimte.ac.cn) (X. Yao), [xuxx@nimte.ac.cn](mailto:xuxx@nimte.ac.cn) (X. Xu).

greatly expanded the market of lithium secondary batteries. However, the wide application of lithium ion batteries is mainly restricted by the safety problem due to extensive use of inflammable organic ethers electrolytes [2]. As an alternative option, all-solid-state lithium batteries (ASSLiBs), utilizing non-flammable inorganic materials as solid electrolytes, could provide an ultimate solution to solve the safety issue of lithium ion batteries [3,4].

The electrochemical performances of ASSLiBs are highly related with the ionic conductivity of solid electrolytes, cathode materials and the interfacial impedance between solid electrolyte and cathode. Up to now, the sulfide-based solid electrolytes such as  $\text{Li}_{3.25}\text{Ge}_{0.25}\text{P}_{0.75}\text{S}_4$ ,  $x\text{Li}_2\text{S}-(1-x)\text{P}_2\text{S}_5$ , and  $\text{Li}_{10}\text{GeP}_2\text{S}_{12}$ , exhibit lithium ion conductivities in the order of  $10^{-3}$  to  $10^{-2}$   $\text{S cm}^{-1}$  at room temperature [5–7], which is comparable to the liquid organic electrolytes. Therefore, the lithium ion conductivity of solid electrolytes may not be the main obstacle in ASSLiBs.

As for positive materials in ASSLiBs with sulfide solid electrolytes, most studies emphasized on  $\text{LiCoO}_2$  intercalation compounds despite their limited discharge capacity ( $\sim 120$   $\text{mAh g}^{-1}$ ) [4,8,9]. By comparison,  $\text{LiNi}_{0.8}\text{Co}_{0.15}\text{Al}_{0.05}\text{O}_2$  (NCA) is feasible to exhibit a higher discharge capacity with lower cost [10], and is suitable to improve the energy density of solid-state lithium cells [11]. However, the discharge capacity of NCA in ASSLiBs is largely reduced due to the large interfacial resistance between the NCA and sulfide electrolytes compared with that in lithium ion batteries with liquid electrolytes [12–14]. Besides the space charge layer and structure deterioration induced by element co-diffusion [12,15], the high interfacial impedance could be attributed to the poor physical contact of solid powders [13,16] and surface defects (or impurities) of positive materials [14,15]. Some efficient strategies have been conducted to reduce the interfacial resistance between cathode and electrolyte [11,13,16,17]. The NCA particles with a surface coating of  $\text{Li}_4\text{Ti}_5\text{O}_{12}$  were synthesized by Seino et al. and used as cathode in ASSLiBs with 70% $\text{Li}_2\text{S}$ –30% $\text{P}_2\text{S}_5$  glass ceramic solid electrolyte. The results state that the interfacial resistance is significantly reduced compared with that of uncoated NCA, resulting in an improved high rate capability [11]. Visbal reported that eliminating absorbed impurities on NCA surface by heating NCA powders at 250 °C in vacuum could reduce the interfacial resistance as well [17]. In our previous study [18], it is found that the interfacial resistance is also affected by the ionic conductivity of solid electrolytes in ASSLiBs with NCA cathode. The  $\text{Li}_{10}\text{GeP}_2\text{S}_{12}$  solid electrolyte not only displays a higher ionic conductivity than that of  $\text{Li}_{3.25}\text{Ge}_{0.25}\text{P}_{0.75}\text{S}_4$  solid electrolyte, but also has lower interfacial resistance with NCA positive material, leading to better electrochemical performances including rate capability and cycling stability as well as low temperature performances. However, the effect of cathode structure and morphology (i.e. particle size, surface impurities and defects as well as morphology) on the electrochemical performances in ASSLiBs is still not set up and unclear.

In this work, a systematical investigation on the fundamental lithium storage behavior of NCA in ASSLiBs was carried out. The relationship between electrochemical performances and NCA structure and morphology was revealed. Ball-milling followed by post-annealing are applied to decrease the particle size and surface defects, which could improve physical contacts and interface chemical stability between the NCA particles and sulfide solid electrolyte, giving rise to a significantly improved electrochemical performances. The results provided new insight for improving the lithium storage capability of NCA cathode in ASSLiBs, which could be also applied in the other cathode systems for ASSLiBs.

## 2. Experimental

The  $\text{Ni}_{0.8}\text{Co}_{0.15}\text{Al}_{0.05}(\text{OH})_2$  precursor (Jintian New Energy Co.,

Ltd.) was mixed with  $\text{LiOH}\cdot\text{H}_2\text{O}$  (99.9%, Aladdin Chemistry. Co., Ltd.) in the mortar with a molar ratio of 1/1.02. The mixture was preheated at 500 °C for 6 h, and subsequently sintered at 700 °C, 750 °C or 800 °C for 12 h in a continuous oxygen flow. The as-sintered samples were named as S700, S750 and S800 respectively. The sample S750 was ground by ball-milling for 10 h in ethanol using a planetary ball mill apparatus, and then dried at 80 °C (labeled as S750-m). The sample S750-m was divided into three parts, which were annealed at the temperature of 700 °C, 750 °C, and 800 °C for 5 h in oxygen, respectively. Accordingly, the post-annealed samples were denoted as PA700, PA750, and PA800.

X-ray diffraction (XRD) measurements were employed to characterize the structure of samples on Bruker AXS D8 Advance diffractometer with  $\text{Cu K}\alpha$  radiation ( $\lambda = 1.54178$  Å). The morphology was analyzed by S-4800 field emission scanning electron microscopy (FE-SEM). Raman spectra were measured with a Renishaw in Via-Reflex Raman spectrophotometer using the 532 nm spectra. X-ray photoelectron spectra (XPS) were collected on a Kratos AXIS ULTRA<sup>DL</sup> X-ray photoelectron spectrometer. The spectrum fitting was applied with CasaXPS software.

$\text{Li}_{10}\text{GeP}_2\text{S}_{12}$  was used as the solid electrolyte for the assembly of ASSLiBs. The  $\text{Li}_{10}\text{GeP}_2\text{S}_{12}$  solid electrolytes was prepared by solid-state reaction method and the details of  $\text{Li}_{10}\text{GeP}_2\text{S}_{12}$  can be found elsewhere [18]. For the composite cathode, the as-synthesized NCA powder was mixed with the  $\text{Li}_{10}\text{GeP}_2\text{S}_{12}$  solid electrolytes in weight ratio of 70:30 using an agate mortar. Li-In alloy foil (99.9%, Alfa Aesar) was used as a counter electrode. ASSLiBs of Li-In/ $\text{Li}_{10}\text{GeP}_2\text{S}_{12}$ /NCA were fabricated as follow: 100 mg of the  $\text{Li}_{10}\text{GeP}_2\text{S}_{12}$  electrolyte was first placed into a teflon tube of 10 mm in diameter to make an electrolyte layer at 240 MPa. Then, 7 mg of the above cathode composite powder was uniformly spread onto the electrolyte layer and pressed at the same pressure. Li-In alloy used as counter electrode was similarly placed on the other side of the electrolyte layer. At last, the all components were compressed together at 360 MPa. The cells were charged and discharged in a galvanostatic mode at room temperature. As the potential of Li-In alloy is 0.62 V vs  $\text{Li/Li}^+$ , the cut-off voltage was set to be 3.7–2.3 V. The current rate of charge/discharge is 0.1C ( $1\text{C} = 120$   $\text{mA g}^{-1}$ ). Electrochemical impedance spectroscopy (EIS) analysis was carried out after the cell was charged to 3.7 V for the second time on a Solartron 1470 E multi-channel potentiostats electrochemical workstation in a frequency range from 0.1 to  $10^6$  Hz with the amplitude of 10 mV.

Electrochemical performances of S750, S750-m and PA750 samples in lithium-ion batteries with the liquid electrolyte were carried out with a CR2023-type coin cell as described in previous work [19]. The working electrode was composed of 80 wt% active materials, 10 wt% polyvinylidene fluoride (PVDF) and 10% acetylene black. Lithium metal was used as counter electrodes. The coin cells were assembled in an argon-filled glove box with 1 M  $\text{LiPF}_6$  in EC and DMC (LB-301, China) as the electrolyte and Celgard 2600 as the separator. The cells were charged and discharged in a galvanostatic mode at room temperature. The cut-off voltage was set to be 3.0–4.3 V and the current rate of charge/discharge is 0.1C ( $1\text{C} = 180$   $\text{mA g}^{-1}$ ).

## 3. Results and discussion

Fig. 1 shows the powder XRD patterns of NCA obtained at different experimental conditions. All the reflections are indexed as a hexagonal lattice of  $\alpha\text{-NaFeO}_2$  structure with a  $R\bar{3}m$  space group [20,21], and no extra diffraction peaks are observed. Clearly, the XRD patterns show the splits of peaks (006)/(102) and (008)/(110), which is the characteristic of a highly ordered layered structure [22]. Besides, the layered structure is further confirmed with the

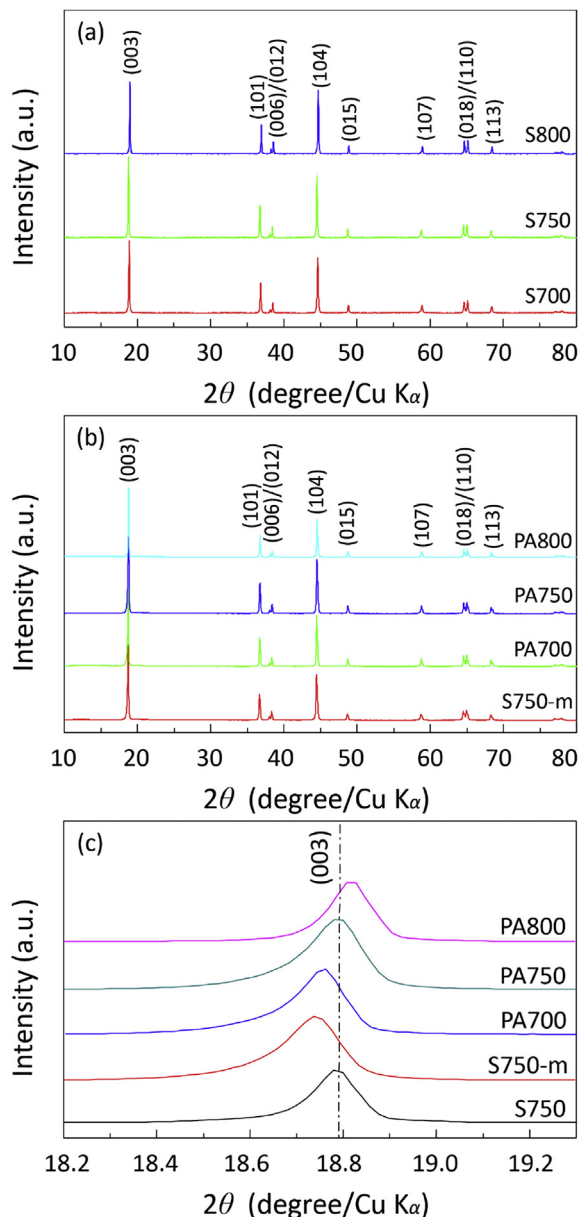


**Fig. 1.** XRD Patterns of NCA powders: (a) S700, S750 and S800; (b) S750-m, PA700, PA750 and PA800; (c) magnified XRD patterns of S750, S750-m, PA700, PA750 and PA800 samples in  $2\theta$  range of  $18.2^{\circ}$ – $19.4^{\circ}$ .

lattice constant ratios of  $c/a$ , which are larger than 4.9 for all samples [23], as listed in Table 1. Moreover, it is known that the integrated intensity ratio of  $I(003)/I(104)$  (defined as  $R$ ) is sensitive to the cation mixing in the lattice and usually used to measure the

**Table 1**  
Structure parameters of all  $\text{LiNi}_{0.8}\text{Co}_{0.15}\text{Al}_{0.05}\text{O}_2$  samples synthesized under different conditions.

Sample	$a$ (Å)	$c$ (Å)	$c/a$	$R$
S700	2.8626	14.1588	4.9462	1.14
S750	2.8659	14.1759	4.9473	1.10
S800	2.8612	14.1462	4.9441	1.01
S750-m	2.8684	14.1836	4.9447	1.15
PA700	2.8667	14.1778	4.9457	1.49
PA750	2.8657	14.1753	4.9465	1.46
PA800	2.8650	14.1646	4.9440	1.45

degree of cation mixing in the series of layered oxide materials. Generally,  $R < 1.2$  means undesirable cation mixing [24]. Here, the  $R$  values for all untreated samples (S700, S750, S800) were lower than 1.2 (as shown in Table 1), which indicated that the samples had undesirable cation mixing. The morphologies of NCA were observed by FE-SEM, as shown in Fig. 2. S700, S750 and S800 samples are comprised of spherical secondary particles with a size of 5–10  $\mu\text{m}$ , which are composed of primary particles with a size of 100–500 nm. And the size of primary particles grows up with the increase of sintering temperatures.

The initial charge/discharge voltage profiles for S700, S750 and S800 samples are shown in Fig. 3. The specific discharge capacity of S700, S750 and S800 are only  $46.7 \text{ mAh g}^{-1}$ ,  $51 \text{ mAh g}^{-1}$ ,  $37 \text{ mAh g}^{-1}$ , respectively. All samples exhibit an inferior specific capacity, which could be attributed to the undesired cation mixing, inappropriate particle size distribution and morphology as observed above. In order to further understand and improve the lithium storage behavior, S750 samples are selected to be ball-milled and post annealed for deeper investigation.

After further ball-milling and post-annealing, the  $R$  values for PA700, PA750 and PA800 samples were significant higher than 1.2 (Table 1), suggesting effectively decrease the undesirable cation mixing. Furthermore, the cell parameters  $c$  firstly increase with the sintering temperature and then decrease with the increasing of post-annealed temperature, as shown in Fig. 1c and Table 1. XPS measurements of S750, S750-m and PA750 samples were conducted to further understand the changes of nickel on the surface of  $\text{LiNi}_{0.8}\text{Co}_{0.15}\text{Al}_{0.05}\text{O}_2$ . Chemical environment of nickel was analyzed in detail, as shown in Fig. 4, both of  $\text{Ni}^{2+}$  cation and  $\text{Ni}^{3+}$  cation coexist on the surface of S750, S750-m and PA750 samples. The intensity of the peaks corresponding to  $\text{Ni}^{2+}$  cation firstly increase after ball milling and then significantly decrease after post-annealing. The effect of ball-milling and post-annealing on the morphologies of NCA is shown Fig. 5. Obviously, the secondary particles are smashed into small particles by ball-milling process, and the average size is about 1–5  $\mu\text{m}$ . Surface defects such as cracks, pores and small particle are clearly observed on the S750-m particles. The post-annealing at  $700^{\circ}\text{C}$  doesn't change particle size. After post-annealing at  $700^{\circ}\text{C}$ , most surface defects have been eliminated, but some residual cracks and vague surface are observed. With higher post-annealing temperature of  $750^{\circ}\text{C}$ , small particles are agglomerated into second particles with a size of 3–5  $\mu\text{m}$ . The surface defects of PA750 are fully recovered, and a smooth surface is obtained. When the post-annealing temperature further increases to  $800^{\circ}\text{C}$ , the primary particles of PA800 grow up obviously.

The effect of ball-milling and post-annealing on electrochemical performances of ASSLiBs were systematically studied. Firstly, the electrochemical performances of S750, S750-m and PA750 samples in lithium ion batteries using the liquid electrolyte were tested, as shown in Fig. S1. The initial discharge specific capacities of S750, S750-m, and PA750 samples are  $151.9$ ,  $162.6$  and  $180.1 \text{ mAh g}^{-1}$ , respectively. Clearly, the initial discharge specific capacity can be improved after ball milling, and further enhanced with post-annealing. Fig. 6 shows the initial charge/discharge curves of all NCA samples in ASSLiBs. The details of initial charge/discharge capacity and coulombic efficiency for all samples are given in Table 2. After ball-milling, the samples S750-m showed an increase of discharge capacity, however, the initial coulombic efficiency is still poor. The decrease of particle size would increase the contact area between solid electrolytes and positive electrodes, and consequently give rise to more diffusion channels for lithium ions transfer [25]. Therefore, the increase of discharge capacity could be due to the smaller particle size [26]. After post-annealing at  $700^{\circ}\text{C}$  and  $750^{\circ}\text{C}$  for 5 h, the PA700 and PA750 samples show discharge



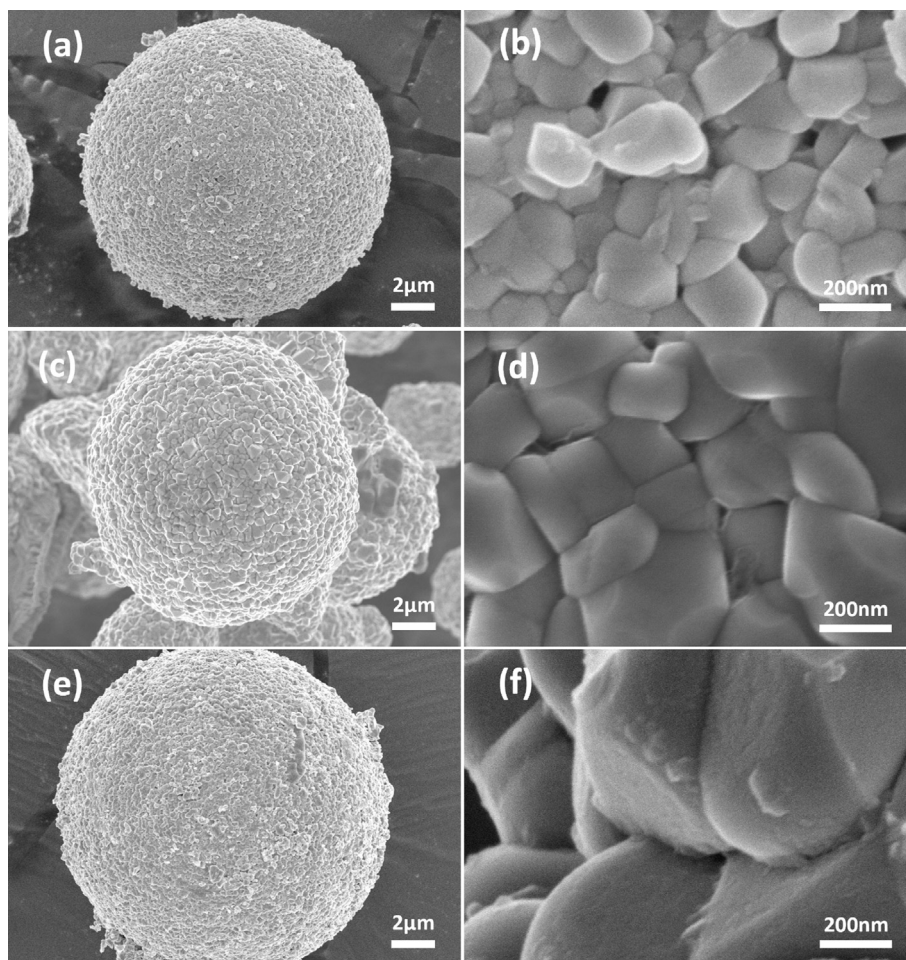


Fig. 2. SEM images of untreated NCA powders: (a, b) S700; (c, d) S750; (e, f) S800.

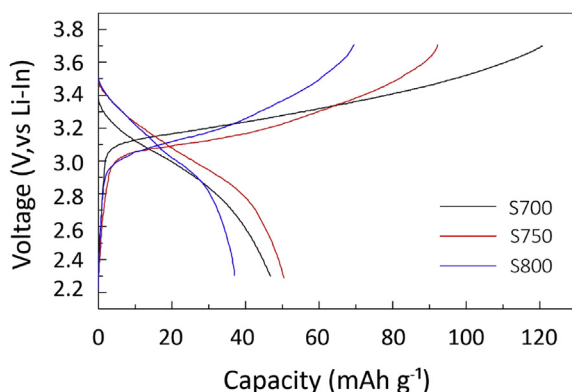


Fig. 3. Initial charge/discharge curve for S700, S750 and S800 samples.

capacities of 118.9 and 145.8  $\text{mAh g}^{-1}$ , respectively, and the corresponding initial coulombic efficiency is up to 68.5% and 76.3%, higher than these reported recently [17]. The lower discharge capacity and initial coulombic efficiency for PA700 are due to incompletely recovered structure and surface defects. However, the initial coulombic efficiency is only 59.3% when the post-annealing temperature is increased to 800 °C. The ball-milling introduces surface defects such as cracks, pores and small particles, while the post-annealing could remove damages caused by the ball-milling

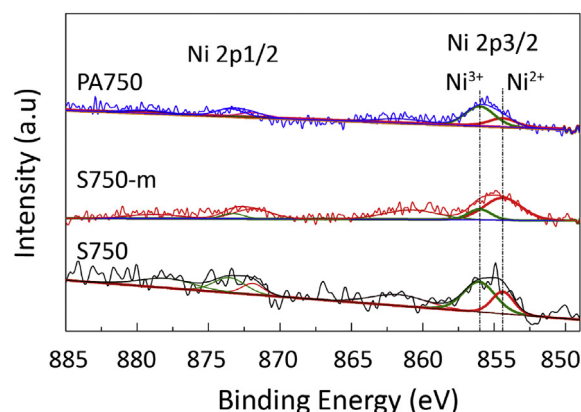
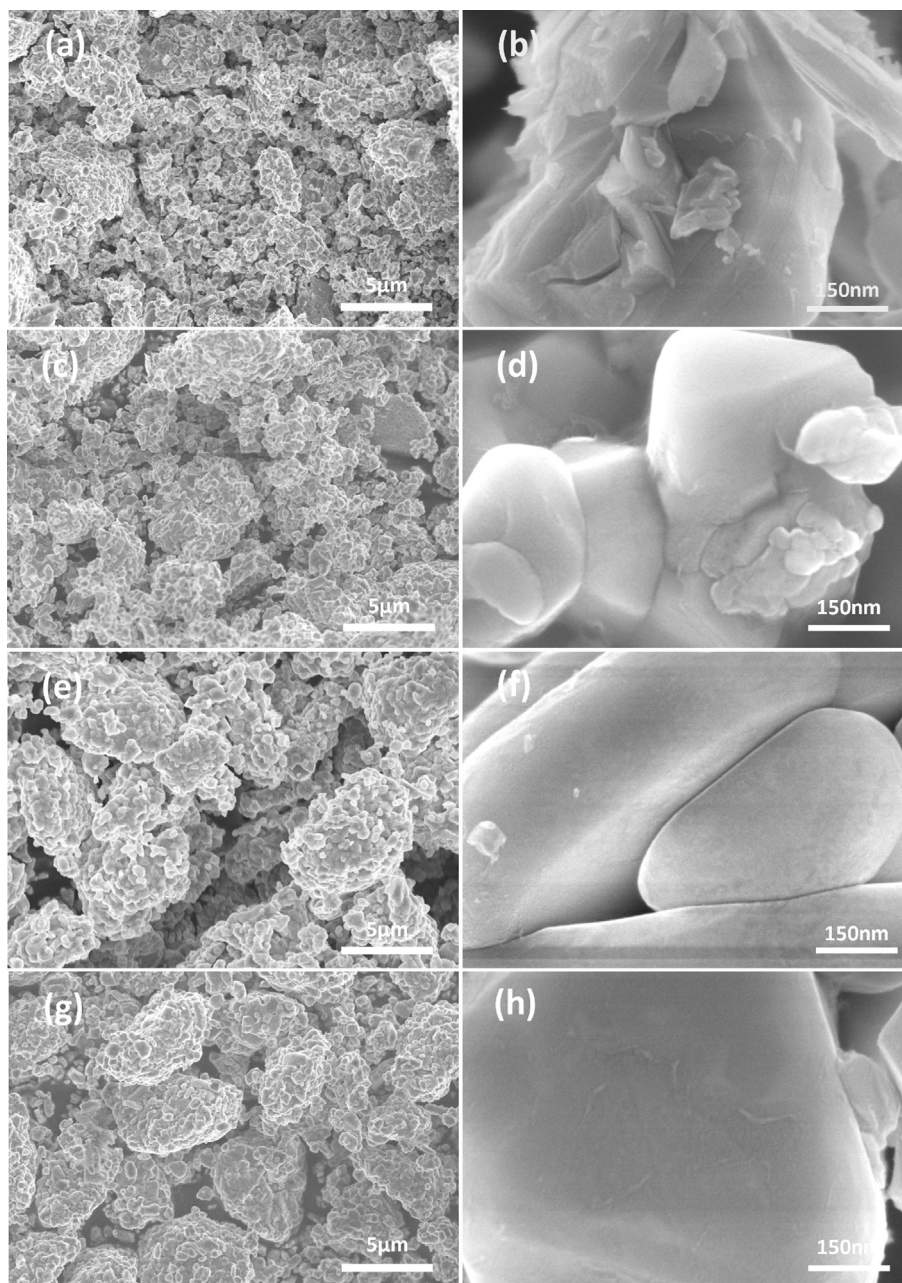


Fig. 4. XPS spectra of Ni 2p<sub>1/2</sub>, Ni 2p<sub>3/2</sub> for the S750, S750-m, and PA750 samples.

and result in reconstruction of the surface structure, as shown in Fig. 5. Therefore, the improvement of discharge capacity for PA750 is ascribed to the surface reconstruction. The effect of surface recovery has been reported for LiCoO<sub>2</sub> and LiNi<sub>1/3</sub>Co<sub>1/3</sub>Mn<sub>1/3</sub>O<sub>2</sub> [27,28]. Since the particle size and surface morphology of PA750 and PA800 samples are very similar, the deterioration of discharge capacity for PA800 is mainly attributed to the growth of primary particles at higher temperature as well as cation mixing [20]. Clearly, 750 °C is the optimal temperature for post-annealing, at



**Fig. 5.** SEM images of processed NCA powders at different experimental condition: (a, b) S750-m; (c, d) PA700; (e, f) PA750 and (g, h) PA800.

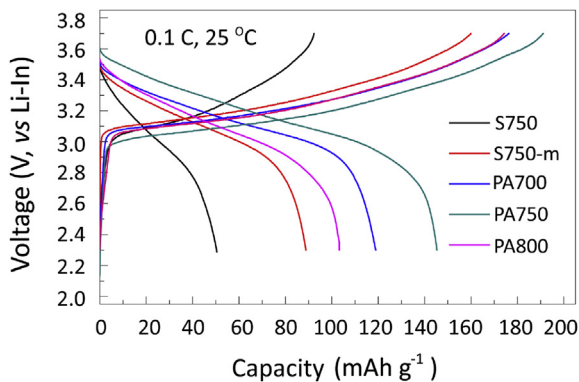
which the surface defects caused by ball-milling could recover well, and meanwhile the cation mixing is appropriate.

Fig. 6 shows the impedance profiles of the all-solid-state cells at the state of second charge to 3.7 V vs. Li-In alloy. The impedance profiles of all the cells consist of a semi-circle in the high-medium frequency region and a straight line in the low frequency region. The intersection point with the horizontal axis in the high frequency ( $1.2 \times 10^5$  Hz) was ascribed to the solid electrolyte layer impedance  $R_{SE}$ . The semi-circle observed in the medium-frequency region is regarded as an interfacial charge transfer resistance ( $R_{PE}$ ), which reflects the interfacial impedance between positive electrode and solid electrolyte interface [12,14]. All the samples had the similar  $R_{SE}$  value (60–70  $\Omega$ ) since they used the same solid electrolyte. However, sample S750, S750-m, PA700, PA750, and PA800 have  $R_{PE}$  values of 830  $\Omega$ , 612  $\Omega$ , 423  $\Omega$ , 252  $\Omega$ , and 497  $\Omega$ ,

respectively. This indicated that the ball milling could reduce the interface resistance a little, and the ball milling together with the post-annealing at moderate temperature could effectively reduce the interface resistance. The results are consistent very well with SEM images and charge/discharge curves. From Figs. 6 and 7, it could be concluded that the higher initial discharge capacity and coulombic efficiency of NCA is closely related to the decrease in the interfacial resistance. Thus, the good distributions of particles caused by ball-milling increase the contact areas between positive electrode and solid electrolyte, and a fresh reconstruction surface facilitate both fast lithium ion and electron conduction at the interface.

In addition to the results of cell impedance, in order to further identify the effect of the ball-milling and post-annealing on the initial discharge capacity of the all-solid-state cells, the micro-





**Fig. 6.** Initial charge/discharge curve for NCA powders S750, S750-m, PA700, PA750 and PA800.

**Table 2**

The initial charge/discharge specific capacity and initial Coulombic efficiency (ICE) corresponding to Figs. 3 and 5.

Samples	Charge (mAh g <sup>-1</sup> )	Discharge (mAh g <sup>-1</sup> )	ICE (%)
S700	114	46.7	40.9
S750	92	51	55
S800	70	37	53
S750-m	160	89	56
PA700	174	119	68
PA750	191	146	76
PA800	174	103	59

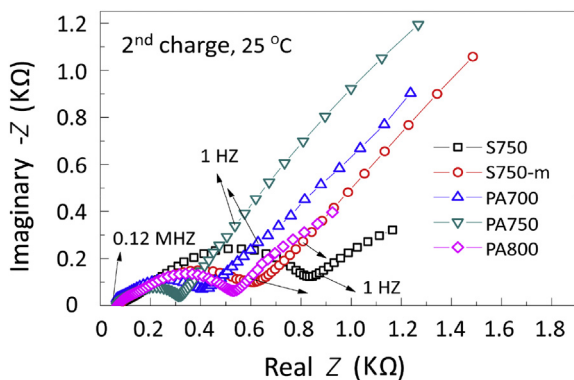


**Fig. 7.** Nyquist plots of S750, S750-m, PA700, PA750 and PA800 at the second charge state of 3.7 V vs Li-In alloy anode.

Raman spectra scattering was conducted on sample S750, S750-m, PA700, PA750 and PA800 to investigate the local cation environment. As shown in Fig. 8, a small peak at 1090 cm<sup>-1</sup> is detected only on particles of sample S750, which is assigned to the symmetric stretch ( $\nu_1(A_1')$ ) of CO<sub>3</sub><sup>2-</sup> in Li<sub>2</sub>CO<sub>3</sub> [29], indicating that Li<sub>2</sub>CO<sub>3</sub> formed during sintering. However, the formed Li<sub>2</sub>CO<sub>3</sub> could be eliminated from particles surface by the ball-milling, and would not appear again after post-annealing process. The fresh surface without impurities and defects would decrease the interface impedance. The peaks located at 475 and 554 cm<sup>-1</sup> are associated with vibrations characteristic of O–Ni–O bending ( $\delta(O-M-O)$ , E<sub>g</sub> mode) and Ni–O stretching ( $\nu(NiO_6)$ , A<sub>1g</sub> mode) [30]. The peak at 475 cm<sup>-1</sup> is related to the order structure [31,32], which suggests that the cation mixing results in the decrease of intensity. The intensity of peak at 475 cm<sup>-1</sup> decreases after ball-milling, indicating that the ball-milling process could lead to larger cation mixing. After post

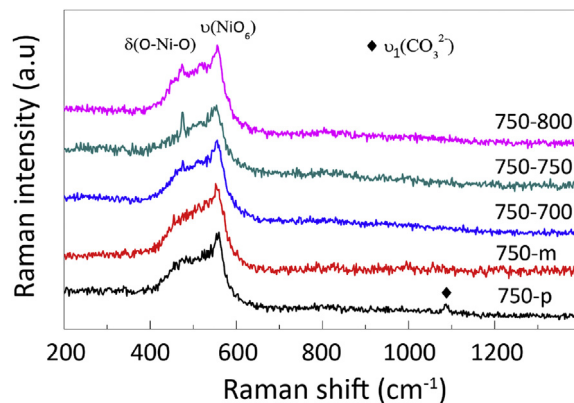


**Fig. 8.** Raman spectra of samples S750, S750-m, PA700, PA750 and PA800.

annealing, the strongest peak (i.e. the lowest cation mixing) is obtained at 750 °C. Thermodynamically, the higher temperature led to the increase in cation mixing [20]. Kinetically, the atoms need thermal energy to rearrange in a limited time. Therefore, a moderate temperature (750 °C) could give the optimal property. The results prove that the decrease of discharge capacity for PA800 is related to the cation mixing.

#### 4. Conclusions

The relationship between fundamental lithium storage behavior of NCA and its structure and morphology in ASSLiBs was revealed. Due to the high interfacial resistance induced by large particle size and surface impurities, the NCA positive material only calcinated at 750 °C show a very low discharge capacity in ASSLiBs. In this case, a ball-milling process followed by post-annealing is carried out and proved to be an efficient way to reduce NCA particle size, recover the surface defects and remove surface impurities. Combination with the XPS and Raman results, ball milling process could increase the surface defects. But S750-m still show improved electrochemical performances compared with S750, which could be mainly ascribed to its reduced particle size. And the further improved electrochemical performance of the PA750 after the post-annealing results from the weakened surface defects and surface impurities. Therefore, the particle size distribution as well as surface defects and impurities of the samples could be the main reason for the ameliorated electrochemical performances. The resultant NCA shows a greatly reduced interfacial resistance with Li<sub>10</sub>GeP<sub>2</sub>S<sub>12</sub> electrolyte, which results in a significantly enhanced discharge capacity of 146 mAh g<sup>-1</sup> at 25 °C in the ASSLiBs.

#### Acknowledgements

The authors are grateful for financial support from the National High Technology Research and Development Program of China, (863 Program, Grant No. 2013AA050906), the National Natural Science Foundation of China (Grant No. 51172250, 51202265), the Strategic Priority Research Program of the Chinese Academy of Sciences (Grant No. XDA09010201) and the Key Scientific and Technological Innovation Team Project of Zhejiang province (Grant No. 2013PT16).

#### Appendix A. Supplementary data

Supplementary data related to this article can be found at <http://dx.doi.org/10.1016/j.jpowsour.2016.01.039>

## References

- [1] J.B. Goodenough, K.-S. Park, *J. Am. Chem. Soc.* 135 (2013) 1167–1176.
- [2] M. Armand, J.M. Tarascon, *Nature* 451 (2008) 652–657.
- [3] K. Takada, *Acta Mater.* 61 (2013) 759–770.
- [4] X. Yao, B. Huang, J. Yin, G. Peng, Z. Huang, C. Gao, D. Liu, X. Xu, *Chin. Phys. B* 25 (2016), 018802.
- [5] F. Mizuno, A. Hayashi, K. Tadanaga, M. Tatsumisago, *Adv. Mater.* 17 (2005) 918–921.
- [6] N. Kamaya, K. Homma, Y. Yamakawa, M. Hirayama, R. Kanno, M. Yonemura, T. Kamiyama, Y. Kato, S. Hama, K. Kawamoto, A. Mitsui, *Nat. Mater.* 10 (2011) 682–686.
- [7] J.E. Trevey, Y.S. Jung, S.-H. Lee, *Electrochim. Acta* 56 (2011) 4243–4247.
- [8] J.G. Kim, B. Son, S. Mukherjee, N. Schuppert, A. Bates, O. Kwon, M.J. Choi, H.Y. Chung, S. Park, *J. Power Sources* 282 (2015) 299–322.
- [9] M. Tatsumisago, M. Nagao, A. Hayashi, *J. Asian. Ceram. Soc.* 1 (2013) 17–25.
- [10] S.-B. Son, J.E. Trevey, H. Roh, S.-H. Kim, K.-B. Kim, J.S. Cho, J.-T. Moon, C.M. DeLuca, K.K. Maute, M.L. Dunn, H.N. Han, K.H. Oh, S.-H. Lee, *Adv. Energy Mater.* 1 (2011) 1199–1204.
- [11] Y. Seino, T. Ota, K. Takada, *J. Power Sources* 196 (2011) 6488–6492.
- [12] N. Ohta, K. Takada, L. Zhang, R. Ma, M. Osada, T. Sasaki, *Adv. Mater.* 18 (2006) 2226–2229.
- [13] H. Kitaura, A. Hayashi, T. Ohtomo, S. Hama, M. Tatsumisago, *J. Mater. Chem.* 21 (2011) 118–124.
- [14] A. Sakuda, A. Hayashi, M. Tatsumisago, *Chem. Mater.* 22 (2010) 949–956.
- [15] A. Sakuda, N. Nakamoto, H. Kitaura, A. Hayashi, K. Tadanaga, M. Tatsumisago, *J. Mater. Chem.* 22 (2012) 15247–15254.
- [16] J. Kim, M. Eom, S. Noh, D. Shin, *J. Power Sources* 244 (2013) 476–481.
- [17] H. Visbal, S. Fujiki, Y. Aihara, T. Watanabe, Y. Park, S. Doo, *J. Power Sources* 269 (2014) 396–402.
- [18] J. Yin, X. Yao, G. Peng, J. Yang, Z. Huang, D. Liu, Y. Tao, X. Xu, *Solid State Ionics* 274 (2015) 8–11.
- [19] G. Peng, L.-L. Zhang, X.-L. Yang, S. Duan, G. Liang, Y.-H. Huang, *J. Alloys Compd.* 570 (2013) 1–6.
- [20] T.-J. Park, J.-B. Lim, J.-T. Son, *Bull. Kor. Chem. Soc.* 35 (2014) 357–364.
- [21] W. Li, J.N. Reimers, J.R. Dahn, *Solid State Ionics* 67 (1993) 123–130.
- [22] T. Ohzuku, A. Ueda, M. Nagayama, *J. Electrochem. Soc.* 140 (1993) 1862–1870.
- [23] L. Ling, N. Zhang, K. Sun, T. Yang, *J. Phys. Chem. Solids* 70 (2009) 727–731.
- [24] C.-H. Lu, B.-J. Shen, *J. Alloy. Compd.* 497 (2010) 159–165.
- [25] H. Kitaura, A. Hayashi, K. Tadanaga, M. Tatsumisago, *J. Power Sources* 189 (2009) 145–148.
- [26] S. Huang, Z. Wen, J. Zhang, X. Yang, *Electrochim. Acta* 52 (2007) 3704–3708.
- [27] H. Meng, B. Huang, J. Yin, X. Yao, X. Xu, *Ionics* 21 (2015) 43–49.
- [28] X. Xu, K. Takada, K. Watanabe, I. Sakaguchi, K. Akatsuka, B.T. Hang, T. Ohnishi, T. Sasaki, *Chem. Mater.* 23 (2011) 3798–3804.
- [29] M.H. Brooker, J.B. Bates, *J. Chem. Phys.* 54 (1971) 4788–4796.
- [30] C. Julien, *Solid State Ionics* 136 (2000) 887–896.
- [31] S. Sivaprakash, S.B. Majumder, *J. Alloy. Compd.* 479 (2009) 561–568.
- [32] S. Sivaprakash, S.B. Majumder, R.S. Katiyar, *J. Electrochem. Soc.* 156 (2009) A328–A333.